Journal of Materials Chemistry A

Accepted Manuscript

ROYAL SOCIETY OF CHEMISTRY

www.rsc.org/materialsA

Journal Name

ARTICLE

Pseudocapacitive behaviours of $Na_2Ti_3O_7$@CNT coaxial nanocables for high-performance sodium-ion capacitors

Received 00th January 20xx,
Accepted 00th January 20xx

DOI: 10.1039/x0xx00000x

www.rsc.org/

Shengyang Dong, Laifa Shen, Hongsen Li, Ping Nie, Yaoyao Zhu, Qi Sheng and Xiaogang Zhang*

Hybrid sodium-ion capacitors (NICs) have tremendous potential in large-scale energy storage applications due to its low-cost, long-lifetime and high-power. However, it remains enormous challenge to find a desired anode material with fast kinetics and superior cycle life. Here an applicable strategy to *in-situ* grow $Na_2Ti_3O_7$ on 1D CNTs is presented as an anode material for sodium-ion capacitors. Benefiting from the unique 1D nanostructure and the presence of pseudocapacitive charge storage mechanism, the $Na_2Ti_3O_7$@CNT electrode exhibits excellent electrochemical performance with high rate capability and superb cycling stability. Moreover, a high performance hybrid NIC is also fabricated by using $Na_2Ti_3O_7$@CNT as an anode and activated carbon derived from outer peanut shell as a cathode, which delivers high energy density (58.5 Wh kg^{-1}), high power density (3000 W kg^{-1}), and long term cycle life (retains *ca*. 75% of its original capacity at 0.4 A g^{-1} after 4000 cycles).

Introduction

Low-cost, long-lifetime, high-power and efficient electrochemical energy storage (EES) systems play an increasingly crucial role in renewable energy and electrified devices, such as aerospace, electric vehicles (EVs) and uninterruptible power system (UPS).[1-7] Due to sodium's low-cost and ubiquitous distribution, Na-based energy storage systems are ideal alternative to the well-known Li-based energy storage technologies.[8-10] However, the broader application of energy storage devices including supercapacitors and batteries is still limited by various drawbacks. Supercapacitors (SCs) possess high power density and long cycle life, but suffer from low energy density.[11, 12] In contrast, sodium-ion batteries (NIBs) provide higher energy density but with low power density and insufficient cycling lifetime.[13, 14] Accordingly, extensive efforts have been devoted to structuring a high-performance device with high energy density, improved power density, and durable cycling stability.[15, 16]

The hybrid sodium-ion capacitor (NIC) is a novel energy storage device that is a bridge in energy and power between NIBs and SCs.[17, 18] As a rule thumb, the NIC couples a capacitor-style material as cathode (positive electrode) and a battery-style material as anode (negative electrode). Sodium-ions insertion/extraction and electric double layer formation with anion (such as ClO_4^-) together provide the high energy and power capability in this hybrid device. In general, sodium-ion insertion/extraction stores charge into the bulk of the anodes more kinetically sluggish than anion adsorption/desorption process onto the surface of the cathodes. Thus, researchers have mainly focused on enhancing the kinetics of sodium insertion/extraction of anode in order to catch up with the fast kinetics of capacitor-style cathode. In addition, Na-based materials operate at voltages of *ca*. 0.3 V which is lower than that of Li-based analogues. This means that Na-related materials may be more suitable for anodes in the hybrid devices.[18] So far, several NIC devices have been fabricated, for instance, AC//Na-TNT,[18] graphite//Na-TNT,[19] AC//V_2O_5/CNT,[20] and AC//$NiCo_2O_4$.[21]

Ti-based oxides have been regarded as attractive anode materials due to their low cost, natural abundance and low toxicity.[22-24] Specially, layered sodium titanate ($Na_2Ti_3O_7$) can reversibly uptake sodium at the lowest voltage (*ca*. 0.3 V *vs*. Na^+/Na) ever reported for oxides insertion anodes.[25] This means that $Na_2Ti_3O_7$ may be very suitable for anode in NICs. However, its low electronic conductivity and structural instability of the intercalated phase result in the unsatisfied rate and cyclic capability.[26, 27] In order to enhance the kinetics of sodium insertion/extraction and cycle stability of the host $Na_2Ti_3O_7$, extensive efforts have been focused on tailoring the particle size to nanoscale,[26] forming a composite with carbon,[28] and structuring novel architecture.[29]

Recently, pseudocapacitive charge storage, a faradaic process involving surface (even bulk) redox reaction, provides a desired mechanism of achieving superior high-rate performance and cycling stability.[30-32] It is limited by surface

Jiangsu Key Laboratory of Materials and Technology for Energy Conversion, College of Material Science and Engineering, Nanjing University of Aeronautics and Astronautics, Nanjing, 210016, P. R. China. E-mail: azhangxg@nuaa.edu.cn; Fax: +86 025 52112626; Tel: +86 025 52112902

† Electronic Supplementary Information (ESI) available: SEM and TEM of pristine $Na_2Ti_3O_7$. N_2 adsorption-desorption isotherms of NTO@CNT, pore size distribution. Electrochemical performance of CNTs. Nyquist plots of NTO@CNT and pristine NTO. Log *i vs.* log *v* and $iv^{-1/2}$ *vs.* $v^{1/2}$. SEM, HRTEM and BET images of PSC. Electrochemical performance of Na/PSC half-cell. See DOI: 10.1039/x0xx00000x

reaction rather than diffusion-controlled process. Thus, it can be seen as a compensation for the relatively low sodium-ion diffusion in insertion materials (e.g. $Na_2Ti_3O_7$). Nano material with well-defined conductive networks is a critical factor to enhance the reactivity of poorly conductive materials in energy storage. Interestingly, it usually induces additional pseudocapacitive capacity, particularly in Na-storage.[33, 34] We all know that novel nano-hybrid materials composed of nanosized active materials and conductive phases are ideal materials for rapid electronic and ionic transport. As a result, a fast pseudocapacitive energy storage mechanism occurs in this nano-hybrid materials, which is favourable for the high power, high capacity and long-life, simultaneously.[20] On the other hand, due to their unique 1D tubular structure, rapid electronic transport, and their ability to form well-defined conductive networks, carbon nano-tubes (CNTs) have been used as a nanosized framework material for application in efficient EES systems.[35-37]

In order to construct a NIC, the cathode also plays an important role as the anode. Carbonaceous materials like activated carbon, graphene and biomass derived carbons are available for hybrid devices.[38-40] Particularly, utilization of biomass derived carbons is attractive in terms of cost, specific capacity, ease of tailoring for desired applications and availability. Several biomass sources such as waste writing paper, cellulose, potato starch, eucalyptus wood saw dust, peanut shells etc have been obtained.[17, 40, 41] Among them, PSC (peanut shell carbon) with extremely large surface area, hierarchically porous architecture, and high levels of oxygen doping delivers exquisite electrochemical performance as the ion adsorption cathode. Based on the above consideration, we have carbonized out peanut shell and converted it to PSC by performing a KOH activation step like the previous report.[17]

In this work, we report an applicable strategy to *in-situ* grow $Na_2Ti_3O_7$ on 1D CNTs. The efficient reaction process involves the growth of titanium oxides precursor on CNTs, and subsequent conversion into sodium titanate through hydrothermal treatment and calcination. Due to the unique 1D nanostructure, high conductivity and partial pseudocapacitive behaviours, $Na_2Ti_3O_7$@CNT electrode exhibits outstanding rate capability and enhanced cycle stability, suggesting a promising high-rate anode material for NICs.

Experimental section

Preparation of $Na_2Ti_3O_7$@CNT coaxial nanocables

All of the chemicals were of analytical grade and used as purchased without further purification. The TiO_2@CNT nanocable was prepared by a sol-gel method using tetrabutyl orthotitanate (TBOT) as the titanium precursor and benzyl alcohol (BA) as surfactant.[42] Typically, acid-treated multiwalled CNTs (50 mg) were dispersed in 20 mL anhydrous ethanol by sonication for 10 minutes, followed by addition of BA (4 mL) and distilled water (1 mL) and the mixture stirred in an ice bath. TBOT (1 mL) was dissolved in 10 mL anhydrous ethanol and slowly dropped into the above suspension. After stirring for 4 h, the precipitates were collected by vacuum filtration, washed with anhydrous ethanol and then dried at 60 °C overnight. Subsequently, TiO_2@CNT (0.2 g) was stirred in a 30 mL of 5 M NaOH solution for 1 h. Then the suspension was transferred into a 50 mL Tefion-lined stainless-steel autoclave and kept at 150 °C for 10 h before cooling down to room temperature naturally. The precipitate was collected by centrifugation, washed with distilled water until the pH value of 8 was accurately achieved. After being dried at 60 °C overnight, the as-synthesized samples were calcinated at 500 °C for 5 h in argon atmosphere to obtain $Na_2Ti_3O_7$@CNT coaxial nanocables (denoted as NTO@CNT). The pristine $Na_2Ti_3O_7$ was synthesized under the similar conditions except for the absence of multiwalled CNTs in the reaction system. The NTO/CNT (pristine NTO mass: CNT mass was set to 84.5:15.5) was obtained by ball-milled in a planetary ball mill at 400 rpm for 4h.

Preparation of peanut shell carbon

The cathode material, peanut shell carbon (PSC) was prepared from the biomass precursor (outer peanut shell).[17] Typically, the pretreated outer peanut shell (1.2 g), concentrated sulfuric acid (2 mL) and distilled water (40 mL) were sealed in 80 mL Teflon-lined stainless-steel autoclave and kept at 180 °C for 48 h before cooling down to room temperature naturally. The precipitate was collected by vacuum-filtration, washed thoroughly with distilled water, and dried at 60 °C overnight. The dried PSC precursor and KOH, in a mass ratio of 1:3, were thoroughly ground using an agate mortar. Then, the mixtures were calcinated at 800 °C for 1h in an argon flow. The activated samples were washed thoroughly with diluted hydrochloric acid (2 M) and distilled water, and finally dried at 100 °C overnight.

Materials characterization

The crystal structures of the samples were characterized by X-ray diffraction (XRD) (Bruker D8 advance) with Cu-K_α radiation. The microscopic morphologies were investigated using transmission electron microscopy (TEM, JEOL JEM-2100), and field emission scanning electron microscopy (FE-SEM, Hitachi S-4800). TGA was carried out on a NETZSCH (STA 409 PC) thermal analyzer under air atmosphere at a temperature ramp of 10 °C min^{-1} with a temperature range from room temperature to 800 °C. The nitrogen adsorption/desorption measurement was carried on an ASAP-2010 surface area analyzer at liquid nitrogen temperature.

Electrochemical measurement

All the electrochemical characterizations were performed in standard CR2032-type coin cells. The working electrodes were prepared by mixing active material, acetylene black, and polyvinylidene difluoride (PVDF) in N-methyl pyrrolidone (NMP) at 80:10:10 mass ratios and casting the slurry on Al foil. Afterwards, electrodes were dried under vacuum at 110 °C overnight. Na/NTO and Na/PSC half-cells were constructed with Na metal as the counter electrode and reference electrode. PSC//NTO@CNT hybrid NIC was assembled using opposing PSC electrode under the optimized mass rate (NTO@CNT mass: PSC mass was set to 1:2, typically, 1.6 mg: 3.2 mg). The mass ratio of positive electrode to negative electrode was based on the well-known charge balance theory ($q^+ = q^-$). The stored charge can be obtained from the specific

capacity (s) and the mass of the electrode (m), which follows the equation: q = s × m.[43, 44] All the cells were assembled in an argon-filled glove box with a glass microfiber filter (Whatman GF/D) as the separator, and 1 M $NaClO_4$ in a mixture of ethylene carbonate (EC) and propylene carbonate (PC) (v:v = 1:1) with 5 wt% fluoroethylene carbonate (FEC) additive as electrolyte. Galvanostatic charge-discharge measurements were performed at different current densities using a CT2001A cell test instrument (LAND Electronic Co.). The cyclic voltammetry (CV) and electrochemical impedance spectroscopy (EIS) studies were carried out on an electrochemical workstation (CH Instruments, model 660C).

The energy densities (E, Wh kg^{-1}) and power densities (P, W kg^{-1}) of the hybrid NICs were calculated as follows:[45, 46]

$$E = P \times t/3600 \quad (1)$$

$$P = \Delta V \times i \quad (2)$$

$$\Delta V = (V_{max} + V_{min})/2 \quad (3)$$

where t is the discharge time (s), i is the discharge current densities normalized by the total active mass in both electrodes (A g^{-1}), V_{max} is the potential at the beginning of discharge after the IR drop and V_{min} is the potential at the end of discharge (V).

Results and discussion

Morphology and structural analysis

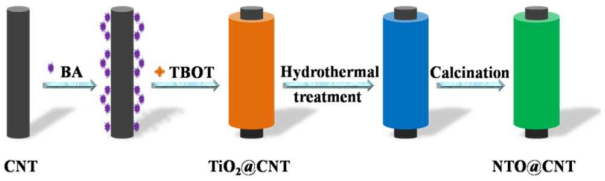

Fig. 1 Schematic illustration of the fabrication processes of NTO@CNT coaxial nanocables.

The formation processes and the resulting symbiotic NTO@CNT coaxial nanocables developed in this paper are schematically illustrated in Fig. 1. First, TiO_2@CNT was prepared by a sol-gel strategy using BA as the surfactant to enhance homogeneous TiO_2 deposition. Then, TiO_2@CNT was transformed into NTO@CNT precursor by hydrothermal treatment in concentrated alkaline solution. Last, the NTO@CNT symbiotic coaxial nanocable was obtained by calcining NTO@CNT precursor under argon atmosphere.

Fig. 2 shows the morphology of acid-treated CNTs, TiO_2@CNT and NTO@CNT, respectively. It is clear to see that acid-treated CNTs product consist of 1D structure with an outer diameter of *ca*. 40-60 nm (Fig. 2a). The morphology of TiO_2@CNT is presented in Fig. 2b, which shows that the nanotubes own smooth surfaces with an outer diameter of *ca*.90-100 nm. It indicates that the TiO_2 layer (ca. 25 nm) had successfully coated on the surface of individual CNTs and formed a core/shell 1D nanostructure. After the treatment with hydrothermal and calcinations, the TiO_2@CNT was converted into NTO@CNT and the unique morphology was maintained simultaneously, which can be demonstrated by SEM images in Fig. 2 (c, d). It should be noted that many open mesopores at the end of NTO@CNT coaxial nanocables (Fig. 2d, marked by arrows). The open porous structures of NTO@CNT can facilitate the transport of sodium-ions, and increase the electrode/electrolyte contact area for fast electrochemical responses. To further investigate the architecture of NTO@CNT coaxial nanocables, the TEM and HRTEM measurements were carried out and the results were depicted in Fig. 2 (e, f). TEM image in Fig. 2e confirms the uniform growth of $Na_2Ti_3O_7$ layer on CNTs. The thickness of $Na_2Ti_3O_7$ sheath is about 25 nm. The 0.84 and 0.34 nm lattice spacing observed in the sheath and core of coaxial nanocable correspond to the (100) crystalline planes of the $Na_2Ti_3O_7$ and the (002) planes of CNTs, respectively (shown in Fig. 2f),[36, 47] thus confirming the successful formation of NTO@CNT coaxial nanocables. In comparison, only atactic bulk $Na_2Ti_3O_7$ were formed under the similar synthesis conditions without the addition of CNTs (Fig. S1, Supporting Information).

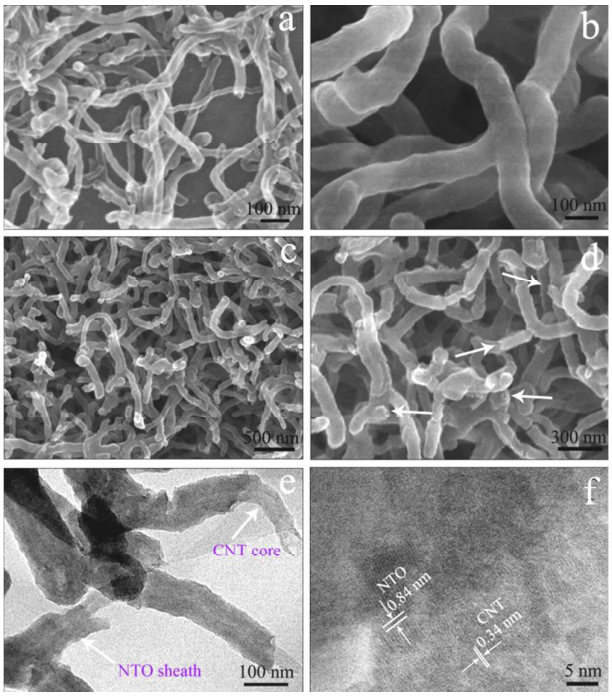

Fig. 2 (a) SEM image of acid-treated CNTs. (b) SEM image of TiO2@CNT. (c) and (d) SEM image of NTO@CNT. (e) TEM image and (f) HRTEM image of NTO@CNT.

Fig. 3a shows the XRD patterns of NTO@CNT coaxial nanocables and pristine NTO. Clearly, all the diffraction peaks is well indexed to the layered $Na_2Ti_3O_7$ (JCPDS card no. 31-1329, S.G.: P21/m, a_o = 9.1279 Å, b_o = 3.8032 Å, c_o = 8.5621 Å).[48] The small diffraction peak (marked by asterisk) at 2ϑ = 26°, which corresponds to the (002) peak of CNTs.[36] The weight fraction of CNTs in NTO@CNT coaxial nanocables was determined by TGA, with the results shown in Fig. 3b. The as-prepared sample shows obvious weight loss at about 600 °C, which is attributed to the combustion of the CNTs. After reaching 800 °C, NTO@CNT shows a total weight loss of 15.5%.

The result indicates that the novel hybrid material compose of 84.5wt% $Na_2Ti_3O_7$ and 15.5wt% CNTs.

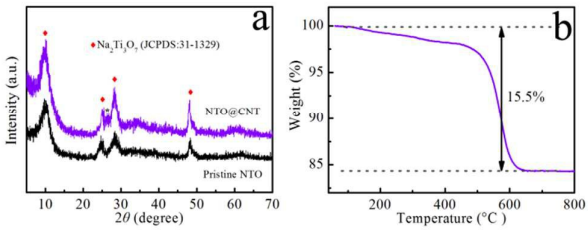

Fig. 3 (a) XRD patterns of NTO@CNT and pristine NTO, (b) TGA of NTO@CNT.

As determined by N_2 adsorption-desorption test (shown in Fig. S2), the prepared NTO@CNT coaxial nanocables possess a high Brunauer-Emmett-Teller (BET) specific surface area of 131.9 m^2 g^{-1}. Besides, the pore sizes are not uniform, which hierarchically distributed in a wide range of 1 to 80 nm. In particular, the pores of below 4 nm are mainly contributed by the interspaces existing in the $Na_2Ti_3O_7$ sheath, the broad distributions ranging from 5 to 80 nm are pores among CNTs or nanocables.

The sodium storage property

Coin-type cell configurations were used to evaluate the sodium storage performance of NTO@CNT and the results were compared with NTO/CNT and pristine NTO anode. Fig. 4a exhibits the capacity-voltage profiles of NTO@CNT in different cycles at a current density of 85 mA g^{-1} in a voltage window of 0.01-2.5 V. The initial discharge and charge capacities are around 587 and 292 mAh g^{-1} (the capacity is calculated based on the weight of the NTO sheath), respectively. The large irreversible capacity loss is mainly attributed to the interfacial reaction between the electrode and the electrolyte, leading to the formation of solid electrolyte interphase (SEI) film.[29, 49] The discharge capacity decrease to 344 mAh g^{-1} while the charge capacity is also up to 286 mAh g^{-1} at the second cycle. The discharge/charge capacities can be kept at about 250 and 230 mAh g^{-1} after 50 and 100 cycles, respectively. Besides, CNTs exhibit quite low capacity (Fig. S3, Supporting Information), indicating that the CNTs make little contribution to the total charge of the hybrid electrode. The electrochemical performance of the three electrodes at multiple-current testing is shown in Fig. 4b. As can be seen, the NTO@CNT electrode delivers discharge capacities of *ca*. 245, 210, 180, 135, 100 mAh g^{-1} under the current densities of 170, 340, 850, 1700, 3400 mA g^{-1}, respectively. Meanwhile, NTO/CNT (pristine NTO) delivers 185 (175), 160 (140), 125 (100), 85 (65) and 60 (40) mAh g^{-1} at the same current rates, respectively. After that, the discharge capacities of the three electrodes can be 230, 165 and 135 mAh g^{-1} when the discharge current density is reduced to 170 mA g^{-1}. As shown in Fig. 4c, a reversible capacity as high as 200 mAh g^{-1} can be remained after 200 cycles at 170 mA g^{-1}. Subsequently, NTO@CNT electrode also delivers *ca*. 145 mAh g^{-1} after another 200 cycles at 850 mA g^{-1}. In contrast, NTO/CNT and pristine NTO electrodes only deliver *ca*. 100 and 85 mAh g^{-1} after 200 cycles at 170 mA g^{-1} (Fig. 4d). More important, as show in Fig. 4e, NTO@CNT electrode shows durable cyclic capacity retention with a high reversible capacity (*ca*. 100 mAh g^{-1}) is retained even after continuous cycling for 1000 cycles at current density of 1700 mA g^{-1}. The above results indicate that the NTO@CNT electrode is apparently superior to other NTO electrodes, as can be seen from the Table S1 (Supporting Information).

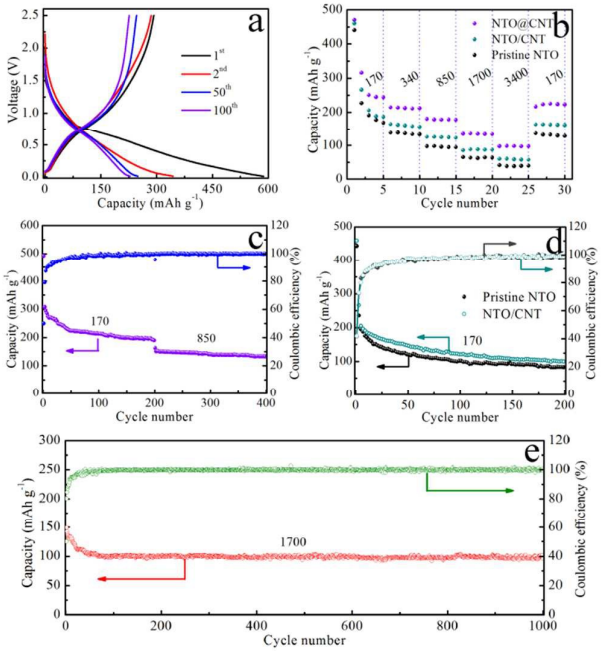

Fig. 4 (a) Capacity-voltage profiles of NTO@CNT in different cycles at 85 mA g^{-1}. (b) Rate performance from 170 to 3400 mA g^{-1} of NTO@CNT, NTO/CNT and pristine NTO. (c) Capacity retention of NTO@CNT at 170 and 850 mA g^{-1} for 200 cycles, respectively. (d) Capacity retention of pristine NTO and NTO/CNT at 170 mA g^{-1} for 200 cycles. (e) Long-term cycling performance at 1700 mA g^{-1}.The current density is based on the weight of NTO sheath or pristine NTO.

To understand the relationship between improved electrochemical performance and electrochemical kinetics, electrochemical impedance spectroscopy (EIS) was carried out. As shown in Fig. S3 (Supporting Information), both Nyquist plots consist of a depressed semicircle in the high frequency region and an oblique straight line in the low frequency region, corresponding to the charge-transfer process at the electrolyte/electrode interface and the solid-state diffusion of sodium ions in the bulk of the electrode, respectively. Obviously, the NTO@CNT electrode exhibits a smaller diameter than those of the corresponding pristine NTO electrode, indicating lower charge-transfer resistance (R_{ct}) and better kinetics for insertion reactions. This result clearly demonstrates that the electronic conductivity has been remarkably enhanced after introducing conducting CNTs into $Na_2Ti_3O_7$. Interestingly, the slope of the Nyquist plot of NTO@CNT electrode is larger than that of pristine NTO electrode in the low frequency region. This may be due to the presence of pseudocapacitive behaviour in NTO@CNT

electrode.[29] More explanations will be shown hereinafter by CV technology.

Kinetics analysis

To further evaluate the electrochemical kinetics of NTO@CNT electrode, CV measurements was carried out at various scan rates from 0.2 to 5 mV s^{-1} as shown in Fig. 5a. The redox peaks represent the sodium insertion/extraction behaviour in the sodium titanate lattice occur at *ca*. 0.25 and 0.55 V. According to the previous approach proposed by Dunn and co-workers,[20, 30, 50] the capacitive contributions of total stored charge can be characterized by analyzing the relationship between the measured current (*i*) and the sweep rate (*v*) from CV data at various sweep rates

$$i = av^b \quad (4)$$

$$\lg i = b \lg v + \lg a \quad (5)$$

where *i* obeys a power law relationship with *v*. Both a and b are the adjustable parameters, with b value can be obtained by the slope of the plot of log *i* *vs*. log *v* according to the equation 5. In particular, b = 0.5 indicates a total diffusion-

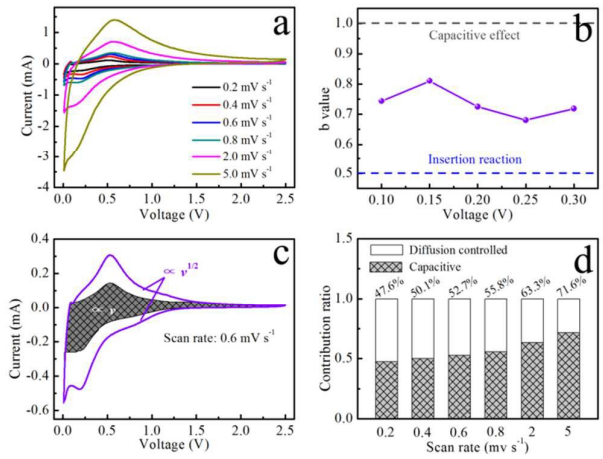

Fig. 5 Kinetics analysis of the electrochemical behavior of NTO@CNT. (a) CV curves with multiple scan rates from 0.2 to 5 mV s^{-1}, (b) b values as a function of voltages during the corresponding anodic CV processes, (c) separation of the capacitive currents (k_1v) and diffusion currents ($k_2v^{1/2}$) in NTO@CNT at a scan rate of 0.6 mV s^{-1}, and (d) the column graphs of contribution ratio of the intercalated and capacitive charge versus scan rate.

controlled (faradaic intercalation) process, whereas b = 1.0 means a capacitive behaviour.[51] The b values around the Na-insertion potentials are shown in Fig. 5b and Fig. S5a (Supporting Information). All the b values are fluctuant close to 0.75, meaning the kinetics of pseudocapacitive contribution. The capacitive contribution can be quantitative distinction from the total charge storage by CV technology. The current response can be expressed as a combination of surface capacitive process and diffusion-controlled intercalation mechanism:[50]

$$i = k_1v + k_2v^{1/2} \quad (6)$$

$$i/v^{1/2} = k_1v^{1/2} + k_2 \quad (7)$$

where k_1v and $k_2v^{1/2}$ represent the current contributions from capacitive process and intercalation mechanism, respectively. Both the parameters k_1 and k_2 at a specific potential are determined from the linear relationship of $iv^{-1/2}$ *vs*. $v^{1/2}$ according to the equation 7 (shown in Fig. S5b, Supporting Information). Thus, the corresponding current contribution can be quantificationally calculated as a function of potential. As shown in Fig. 5c, the capacitive currents (k_1v) are calculated and distinguished from the total measured currents. Apparently, the diffusion-controlled process is mainly generated at around the peak potential, indicating that the diffusion process is facile at this region and corresponds to the redox reaction with Ti^{4+}/Ti^{3+}. Based on the quantitative calculation, *ca*. 52.7% of the total capacity is capacitive contribution at the sweep rate of 0.6 mV s^{-1}. Capacitive contribution ratios at other sweep rates were also calculated and the results as shown in Fig. 5d. Note that the capacitive capacity in NTO@CNT electrode is strongly dependent on the sweep rate. *Ca*. 47.6% of the total stored charge is capacitive at 0.2 mV s^{-1} and finally reaches *ca*. 71.6 % at 5 mV s^{-1}.

Electrochemical performance in hybrid NIC

The SEM and TEM images confirm that PSC exhibits 3D open sponge morphology with a low degree of ordering structure (Fig. S6, Supporting Information). Fig. S7 demonstrates that PSC possesses sizable specific surface areas (1900.5 m^2 g^{-1}) and porosity (0.86 cm^3 g^{-1}). This Na/PSC half-cell delivers super rate capability and cycling stability (Fig. S8, Supporting Information). Multiple-current testing is shown in Fig. S8a. The discharge capacity can be as high as 78.2 mAh g^{-1} at 0.5 A g^{-1}, and the capacity is still remained at 53.9 mAh g^{-1} even at the very high current of 2 A g^{-1}. Moreover, the PSC electrode retained *ca*.85% of the initial capacity after 2000 cycles at 0.5 A g^{-1} (Fig. S8b, Supporting Information).

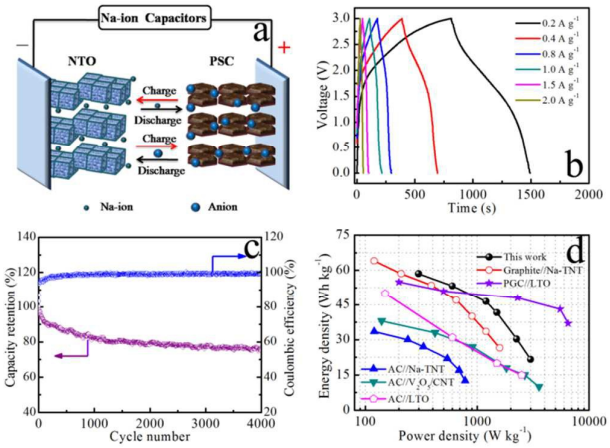

Fig. 6 (a) Schematic diagram of hybrid NICs. (b) Galvanostatic charge-discharge profiles at various current densities. (c) Cycling stability tested at 0.4 A g^{-1} for 4000 cycles. (d) Ragone plots of PSC//NTO@CNT hybrid device compared with other reported hybrid NICs and LICs. The calculated energy and power densities are based on total active mass in both electrodes.

We fabricated a high performance NIC by using NTO@CNT as an insertion-type anode and PSC as adsorption cathode. The schematic diagram and electrochemical performance of PSC//$Na_2Ti_3O_7$@CNT (represented by PSC//NTO@CNT) hybrid NIC are shown in Fig. 6. As seen in Fig. 6a, NTO@CNT anode undergoes Na-insertion, whereas the PSC cathode involves the electric double layer formation with anion (ClO_4^-) across the electrode/electrolyte interface during the charging process. The electrochemical reaction is reversed during the subsequent discharge process. Fig. 6b provides the galvanostatic charge-discharge curves at various current densities. Obviously, the discharge curve is composed of three segments: the first one is IR drop, which mainly attributed to the resistance induced by electrode materials; The second is monotonous curve, which believed to be due to Na^+ extraction from the NTO@CNT anode and desorption of ClO_4^- from the PSC cathode at the same time; And the third one is sudden drop, implying that Faradaic and non-Faradaic reactions have been completed. The cycling performance of the PSC//NTO@CNT hybrid NIC was tested at a current density of 0.4 A g^{-1}. As shown in Fig. 6c, *ca*. 82% of the initial discharge capacity is retained after 1000 cycles, 79% after 2000 cycles, and 75% after 4000 cycles. This indicates that the Faradaic and non-Faradaic reactions occurring at the hybrid system are highly reversible. Fig. 6d offers the Ragone plots of the PSC//NTO@CNT hybrid NIC at room temperature, tested at a voltage window of 0-3 V. The calculated energy and power densities are based on total active mass in both electrodes. It delivers a superb energy density of 58.5 Wh kg^{-1} at a power density of 300 W kg^{-1}. Even at an extremely high power density of 3000 W kg^{-1}, the PSC//NTO@CNT hybrid assembly exhibits a respectable energy density of 21.6 Wh kg^{-1}. Clearly, this electrochemical performance of the PSC//NTO@CNT hybrid NIC is superior to those of hybrid NICs or LICs. Such as, graphite//Na-TNT,[19] AC//Na-TNT,[18] AC//V_2O_5/CNT,[20] AC//LTO,[38] PGC//LTO.[52]

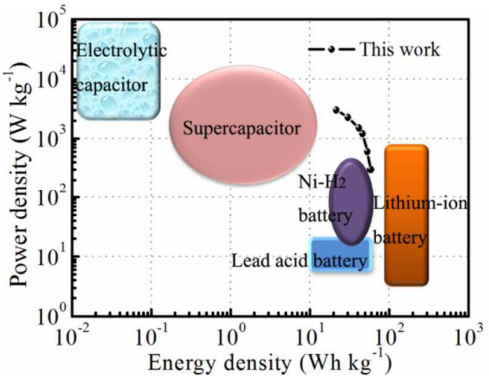

Fig. 7 Ragone plots of PSC//NTO@CNT NIC compared with commercial energy storage devices.

Furthermore, Fig. 7 compares the electrochemical performance of the PSC//NTO@CNT hybrid NIC and commercial energy storage devices, such as, electrolytic capacitors, supercapacitors, Ni-H_2 batteries, lead acid batteries, lithium-ion batteries. Clearly, the PSC//NTO@CNT hybrid NIC has much higher energy density than supercapacitors and even comparable to Ni-H_2 batteries and lead acid batteries, while the power density significantly higher than that of Ni-H_2 batteries and LIBs and can be even compared with supercapacitors.

Conclusions

In summary, NTO@CNT coaxial nanocables were successfully fabricated through sol-gel method and subsequent in-situ chemical sudiation and short calcination. The novel nano-composite exhibits enhanced electrochemical properties. Kinetics analysis reveals an interesting pseudocapacitive behaviour in the NTO@CNT electrode. This pseudocapacitive contribution is highly beneficial to fast Na^+ storage and long-term cyclability. A high performance hybrid NIC is also fabricated by using NTO@CNT as anode and PSC as cathode, which provide a simultaneous improvement in energy (58.6 Wh kg^{-1}), power (3000 W kg^{-1}) and cycle (4000 cycles) performances. More encouragingly, imposing of pseudocapacitive charge storage on typical insertion materials is a promising strategy for developing electrode materials with high power density and long cycle life for NICs.

Acknowledgements

This work was financially supported by the National Basic Research Program of China (973 Program) (No. 2014CB239701), National Natural Science Foundations of China (No. 21173120, 51372116), Natural Science Foundations of Jiangsu Province (No. BK2011030), the Fundamental Research Funds for the Central Universities of NUAA (NP2014403), Outstanding Doctoral Dissertation in NUAA (BCXJ14-10), Jiangsu Innovation Program for Graduate Education (KYLX_0255), and A Project Funded by the Priority Academic Program Development of Jiangsu Higher Education Institutions (PAPD).

Notes and references

1. M. Armand and J.-M. Tarascon, *Nature*, 2008, **451**, 652.
2. C.-P. Yang, Y.-X. Yin and Y.-G. Guo, *J. Phys. Chem. Lett.*, 2015, **6**, 256.
3. Y. Wang, X. Yu, S. Xu, J. Bai, R. Xiao, Y.-S. Hu, H. Li, X.-Q. Yang, L. Chen and X. Huang, *Nat. Commun.*, 2013, **4**, 2365.
4. Z. Chen, Y. Yuan, H. Zhou, X. Wang, Z. Gan, F. Wang and Y. Lu, *Adv. Mater.*, 2014, **26**, 339.
5. H. Li, L. Shen, B. Ding, G. Pang, H. Dou and X. Zhang, *Nano Energy*, 2015, **13**, 18.
6. L. Li, S. Liu and A. Manthiram, *Nano Energy*, 2015, **12**, 852.
7. G. He, L. Li and A. Manthiram, *J. Mater. Chem. A*, 2015, **3**, 14750.
8. S. W. Kim, D. H. Seo, X. Ma, G. Ceder and K. Kang, *Adv. Energy Mater.*, 2012, **2**, 710.
9. P. Nie, Y. Zhu, L. Shen, G. Pang, G. Xu, S. Dong, H. Dou and X. Zhang, *J. Mater. Chem. A*, 2014, **2**, 18606.
10. Y. Zhu, P. Nie, L. Shen, S. Dong, Q. Sheng, H. Li, H. Luo and X. Zhang, *Nanoscale*, 2014, **7**, 3309.

11. L. Shen, J. Wang, G. Xu, H. Li, H. Dou and X. Zhang, *Adv. Energy Mater.*, 2015, **5**, DOI: *10.1002/aenm.201400977*.
12. H. Xu, X. Hu, Y. Sun, H. Yang, X. Liu and Y. Huang, *Nano Res.*, 2015, **8**, 1148.
13. X. Wang, S. Kajiyama, H. Iinuma, E. Hosono, S. Oro, I. Moriguchi, M. Okubo and A. Yamada, *Nat. Commun.*, 2015, **6**, 6544.
14. D. Wu, X. Li, B. Xu, N. Twu, L. Liu and G. Ceder, *Energy Environ. Sci.*, 2015, **8**, 195.
15. V. Aravindan, J. Sundaramurthy, A. Jain, P. S. Kumar, W. C. Ling, S. Ramakrishna, M. P. Srinivasan and S. Madhavi, *Chemsuschem*, 2014, **7**, 1858.
16. N. Arun, A. Jain, V. Aravindan, S. Jayaraman, W. Chui Ling, M. P. Srinivasan and S. Madhavi, *Nano Energy*, 2015, **12**, 69.
17. J. Ding, H. Wang, Z. Li, K. Cui, D. Karpuzov, X. Tan, A. Kohandehghan and D. Mitlin, *Energy Environ. Sci.*, 2015, **8**, 941.
18. J. Yin, L. Qi and H. Wang, *ACS Appl. Mater. Interfaces*, 2012, **4**, 2762.
19. L. Zhao, L. Qi and H. Wang, *J. Power Sources*, 2013, **242**, 597.
20. Z. Chen, V. Augustyn, X. Jia, Q. Xiao, B. Dunn and Y. Lu, *ACS Nano*, 2012, **6**, 4319.
21. R. Ding, L. Qi and H. Wang, *Electrochim. Acta*, 2013, **114**, 726.
22. P. J. P. Naeyaert, M. Avdeev, N. Sharma, H. Ben Yahia and C. D. Ling, *Chem. Mater.*, 2014, **26**, 7067.
23. D. Seshadri, M. Shirpour and M. Doeff, *J. Electrochem. Soc.*, 2015, **162**, A52.
24. Y. Zhang, L. Guo and S. Yang, *Nanoscale*, 2015, DOI: *10.1039/C5NR03076E*.
25. P. Senguttuvan, G. Rousse, V. Seznec, J. M. Tarascon and M. R. Palacin, *Chem. Mater.*, 2011, **23**, 4109.
26. H. L. Pan, X. Lu, X. Q. Yu, Y. S. Hu, H. Li, X. Q. Yang and L. Q. Chen, *Adv. Energy Mater.*, 2013, **3**, 1186.
27. J. Xu, C. Ma, M. Balasubramanian and Y. S. Meng, *Chem. Commun.*, 2014, **50**, 12564.
28. Z. C. Yan, L. Li, H. B. Shu, X. K. Yang, H. Wang, J. L. Tan, Q. Zhou, Z. F. Huang and X. Y. Wang, *J. Power Sources*, 2015, **274**, 8.
29. Y. P. Zhang, L. Guo and S. H. Yang, *Chem. Commun.*, 2014, **50**, 14029.
30. V. Augustyn, J. Come, M. A. Lowe, J. W. Kim, P. L. Taberna, S. H. Tolbert, H. D. Abruna, P. Simon and B. Dunn, *Nat. Materials*, 2013, **12**, 518.
31. Z. Chen, V. Augustyn, X. L. Jia, Q. F. Xiao, B. Dunn and Y. F. Lu, *ACS Nano*, 2012, **6**, 4319.
32. C. Chen, Y. Wen, X. Hu, X. Ji, M. Yan, L. Mai, P. Hu, B. Shan and Y. Huang, *Nat. Commun.*, 2015, **6**, 6929.
33. P. F. Yu, C. L. Li and X. X. Guo, *J. Phys. Chem. C*, 2014, **118**, 10616.
34. G. A. Muller, J. B. Cook, H.-S. Kim, S. H. Tolbert and B. Dunn, *Nano Lett.*, 2015, **15**, 1911.
35. Z. H. Wen, Q. Wang, Q. Zhang and J. H. Li, *Adv. Funct. Mater.*, 2007, **17**, 2772.
36. L. F. Shen, C. Z. Yuan, H. J. Luo, X. G. Zhang, K. Xu and F. Zhang, *J. Mater. Chem.*, 2011, **21**, 761.
37. N. Wang, D. Jiang, L. Ye, M. Murugesan, M. Edwards, Y. Fu and J. Liu, *Adv. Funct. Mater.*, 2015, **25**, 4135.
38. H. Kim, K. Y. Park, M. Y. Cho, M. H. Kim, J. Hong, S. K. Jung, K. C. Roh and K. Kang, *ChemElectroChem*, 2014, **1**, 125.
39. Z. Gao, W. Yang, J. Wang, N. Song and X. Li, *Nano Energy*, 2015, **13**, 306.
40. L. Wei, M. Sevilla, A. B. Fuertes, R. Mokaya and G. Yushin, *Adv. Energy Mater.*, 2011, **1**, 356.
41. B. Senthilkumar, Z. Khan, S. Park, K. Kim, H. Ko and Y. Kim, *J. Mater. Chem. A*, 2015, *DOI: 10.1039/C5TA04737D*.
42. D. Eder and A. H. Windle, *J. Mater. Chem.*, 2008, **18**, 2036.
43. Z. Chen, V. Augustyn, J. Wen, Y. Zhang, M. Shen, B. Dunn and Y. Lu, *Adv. Mater.*, 2011, **23**, 791.
44. H. W. Wang, C. Guan, X. F. Wang and H. J. Fan, *Small*, 2015, **11**, 1470.
45. Y. Wang, Z. Hong, M. Wei and Y. Xia, *Adv. Funct. Mater.*, 2012, **22**, 5185.
46. E. Lim, H. Kim, C. Jo, J. Chun, K. Ku, S. Kim, H. I. Lee, I. S. Nam, S. Yoon, K. Kang and J. Lee, *ACS Nano*, 2014, **8**, 8968.
47. Y. Xu, Y. Zhuang and X. Fu, *J. Phys. Chem. C*, 2010, **114**, 2669.
48. W. Wang, C. Yu, Z. Lin, J. Hou, H. Zhu and S. Jiao, *Nanoscale*, 2013, **5**, 594.
49. A. Rudola, K. Saravanan, C. W. Mason and P. Balaya, *J. Mater. Chem. A*, 2013, **1**, 2653.
50. J. Wang, J. Polleux, J. Lim and B. Dunn, J. Phys. Chem. C, 2007, **111**, 14925.
51. I. E. Rauda, V. Augustyn, B. Dunn and S. H. Tolbert, *Acc. Chem. Res.*, 2013, **46**, 1113.
52. Y. Lei, Z.-H. Huang, Y. Yang, W. Shen, Y. Zheng, H. Sun and F. Kang, *Sci. Rep.*, 2013, **3**, 2477.

Pseudocapacitive behaviours in $Na_2Ti_3O_7$@CNTs enhance the electrochemical performance of Na-ion capacitor with high energy density and high power density.

TOC figure